

Ab initio modeling and experimental investigation of Fe₂P by DFT and spin spectroscopiesPietro Bonfà ^{1,2,*} Muhammad Maikudi Isah ¹ Benjamin A. Frandsen ³ Ethan J. Gibson ³ Ekkes Brück,⁴
Ifanyi John Onuorah ¹ Roberto De Renzi,¹ and Giuseppe Allodi¹¹*Department of Mathematical, Physical and Computer Sciences, University of Parma, 43124 Parma, Italy*²*Centro S3, CNR-Istituto Nanoscienze, 41125 Modena, Italy*³*Department of Physics and Astronomy, Brigham Young University, Provo, Utah 84602, USA*⁴*Fundamental Aspects of Materials and Energy (FAME), Faculty of Applied Sciences,
Delft University of Technology, 2629 JB Delft, The Netherlands*

(Received 10 November 2020; revised 25 February 2021; accepted 30 March 2021; published 26 April 2021)

Fe₂P alloys have been identified as promising candidates for magnetic refrigeration at room-temperature and for custom magnetostatic applications. The intent of this study is to accurately characterize the magnetic ground state of the parent compound, Fe₂P, with two spectroscopic techniques, μ SR and NMR, in order to provide solid bases for further experimental analysis of Fe₂P-type transition metal based alloys. We perform zero applied field measurements using both techniques below the ferromagnetic transition $T_C = 220$ K. The experimental results are reproduced and interpreted using first principles simulations, validating this approach for quantitative estimates in alloys of interest for technological applications.

DOI: [10.1103/PhysRevMaterials.5.044411](https://doi.org/10.1103/PhysRevMaterials.5.044411)**I. INTRODUCTION**

Fe₂P-based alloys have attracted significant research interest in recent years owing to their first-order magnetic transition (FOMT) coupled to a magnetoelastic transition, giving rise to a giant magnetocaloric effect in the vicinity of their Curie temperature [1]. This transition is tunable across room temperature by suitable (Fe,Mn) and (P,Si)/(P,B) substitution [2,3]. Along with their composition by cheap and abundant elements, this makes them eligible for energy transduction applications including solid-state harvesting of thermal energy [4,5] and real-case magnetocaloric refrigerators, that provide increased energy efficiency and substantial environmental benefits compared to gas compression thermodynamic cycles [6–9].

A FOMT is also shown by the parent compound Fe₂P [10], which exhibits a much larger magnetocrystalline anisotropy (MCA) than Fe₂P-based FeMnPSi compounds [11], making it rather a candidate material for permanent magnets. Indeed, its Curie temperature ($T_C \approx 220$ K) is too low for most applications. However, T_C can be raised well above room temperature by suitable Si, Ni, or Co alloying while preserving a MCA nearly as large as in the parent compound [12]. It is therefore apparent that pure Fe₂P, though not directly applicable in magnetic or magnetocaloric technology, shares most of its physics with the derived alloys, while it is possibly a simpler system to model theoretically.

Fe₂P crystallizes in the hexagonal C₂₂ structure with a space group $P\bar{6}2m$ (189). The primitive unit cell contains three formula units and four inequivalent sites, with iron occupying the 3*f* (Fe1) and the 3*g* sites (Fe2) in equal number,

and phosphorus occupying sites 2*c* (P1) and 1*b* (P2) in a 2:1 ratio [13,14]. The compound orders ferromagnetically (FM) with magnetic moments directed along the *c* axis. The magnetic structure of Fe₂P has been widely investigated by neutron scattering and Mössbauer spectroscopy [10,14–19]. All reports qualitatively agreed on a larger Fe2 moment with a localized character, and a reduced Fe1 moment typical of itinerant magnetism (a feature shared by FeMnPSi alloys [20]). However, poor quantitative agreement on the size of the Fe1 magnetic moment characterized early literature and, in addition, the presence of helical states below T_C was discussed [18]. Recently, elastic neutron scattering experiments [21] seem to have finally established the value of the Fe1 and Fe2 moments as 0.8 μ_B and 2.11 μ_B , respectively. The same experiments also showed absence of canting below T_C and the presence of sizable local moments on Fe up to 30 K above the FM transition temperature.

In this work, we present an investigation of the magnetically ordered phase and of the magnetic transition of this compound by two local probes of magnetism, namely NMR and μ SR. Both techniques have been used to probe Fe₂P only in their infancy and published results are very limited to the best of our knowledge [22,23].

In zero applied field (ZF), ³¹P and ⁵⁷Fe nuclei resonate in their hyperfine fields, giving rise to distinct resonance lines for each crystallographic site. We detected the ⁵⁷Fe resonance stemming from Fe2 and the ³¹P resonances of P1 and P2 and unambiguously assigned them to their respective nuclei, thus correcting the peak attribution by an early NMR work [23], which is proven here to be erroneous. The so-determined ³¹P hyperfine fields effectively complement the determination of the ⁵⁷Fe hyperfine fields by Mössbauer spectroscopy [10]. ZF μ SR showed a single sharp precession peak below T_C , whose low-temperature frequency poses stringent constraints to the

*pietro.bonfa@unipr.it

stopping site of the implanted muons, while its temperature dependence confirms a FOMT in the system. Experimental results are compared to a simulation of the system by *ab initio* methods, yielding theoretical predictions for the local fields at the ^{31}P , ^{57}Fe nuclei and at the muon in its stable interstitial site.

The motivation of this work is threefold. First, the inconsistencies that can be found in the sparse and often very old literature on Fe_2P , as pointed out above, demand clarification by newer experiments. Second, this study will guide the interpretation of NMR and μSR experiments on Fe_2P -based alloys of interest for applications. Third, our results benchmark and validate *ab initio* investigations of hyperfine couplings that are shown to be extremely useful for experimental data analysis.

II. MATERIAL AND METHODS

Fe_2P is prepared by firing a mixture of BASF carbonyl iron powder with red phosphorus under protective atmosphere. This mixture reacts exothermally and is very low in transition metal impurities, less than 0.01%. It was checked by x-ray diffraction to be single phase Fe_2P type.

The NMR experiments were carried out by a home-built phase-coherent spectrometer [24] and a resonant LC probehead, using a field-sweeping cold-bore cryomagnet (Oxford Instruments Maglab EXA) equipped with a helium-flow variable temperature insert and a nitrogen-flow cryostat in zero field as sample environments at $T = 5\text{ K}$ and $T \geq 80\text{ K}$, respectively. ZF measurements at 77.3 K were performed by directly immersing the probehead in a liquid nitrogen dewar. In Fe_2P there are actually two distinct ways of performing NMR. The first is, in ZF, exploiting a highly enhanced signal from the nuclei in the domain walls [25,26]. The second records the signal of the nuclei inside the domains. Both these conditions, achieved with distinct excitation regimes and corresponding, respectively, to the application of short and strongly attenuated radio frequency (rf) pulses on one hand, and of longer and much more intense pulses on the other, were identified for the ZF resonance of ^{31}P nuclei. Nevertheless, only the domain wall NMR signals were systematically employed in our ZF investigation, as their low-power excitation is experimentally more convenient. The domain wall signal is progressively extinguished in increasing applied fields, and only signals with similar excitation characteristics as the ZF domain signal are detected in applied fields large enough to saturate the magnetization. Additional details about the experimental determination of these two conditions are reported in the Supplemental Material (SM) [27].

μSR experiments were performed on the LAMPF (Los Alamos Meson Physics Facility) spectrometer at TRIUMF in Vancouver, Canada and the General Purpose Surface-Muon Instrument at the Paul Scherrer Institut (PSI) in Villigen, Switzerland. The loose powder sample of Fe_2P used for the experiment at TRIUMF was loaded into a mylar pouch and placed in a low-background sample holder. μSR spectra were collected in zero field (ZF) at temperatures between 100 K and 300 K using a helium flow cryostat to control the temperature. A calibration measurement was conducted in a weak transverse field at 275 K. The powder sample used at PSI was mixed with a small amount of wax. ZF spectra were collected

at 5 K and 200 K using a helium flow cryostat. At both experimental facilities, data were collected in a warming sequence. Fits to the μSR spectra were conducted via least-squares optimization using MUSRFIT [28] and a home-built python package called BEAMS, both of which yielded statistically indistinguishable results for the oscillating frequencies.

The magnetic and structural stability of Fe_2P and of various alloys have already been studied with different computational approaches [12,29–31]. We reproduced previously reported results on the FM phase [16,17,31,32] with both plane wave and full-potential approaches using the QUANTUM ESPRESSO suite of codes, the WIEN2K package, and the Elk code [33–37]. The plane wave and pseudopotential method is essential to reduce the computational effort required for muon site assignment and hyperfine field characterization, while full potential approaches provide superior accuracy for the evaluation of the hyperfine fields at P nuclei. All computational details are reported in the SM [27].

III. RESULTS

A. NMR

Spontaneous ZF NMR signals were detected at low temperature in the 70–90 MHz and the 13–24 MHz frequency intervals, in loose agreement with the frequency bands where similar resonances were reported by Koster and Turrell and assigned therein to ^{31}P in P1 and P2 and ^{57}Fe in Fe1 and Fe2, respectively [23].

The higher-frequency portion of the ZF spectrum at 5 K is plotted in Fig. 1(a), together with a phenomenological multi-Gaussian fit (solid curve). The relatively high frequency indicates that these resonances stem from ^{31}P nuclei (gyromagnetic ratio $^{31}\gamma/2\pi = 17.2357\text{ MH/T}$), since a ^{57}Fe resonance at the same frequency ($^{57}\gamma/2\pi = 1.3786\text{ MH/T}$) would correspond to hyperfine fields of $\approx 60\text{ T}$, requiring an unphysical local moment $> 5\ \mu_B$ according to the known iron hyperfine coupling [38]. Nuclear spin echoes were excited with shorter and strongly attenuated rf pulses compared to standard NMR in nonmagnetic compounds, indicative of a large rf enhancement of the resonance [25]. The mean enhancement factor η was estimated to be on the order of 1000 by comparison with the optimum excitation conditions in an intense applied field saturating the magnetization (see below), where $1 < \eta < 2$ can be assessed [39]. Such a large η value proves that these signals originate from nuclei in domain walls [40].

The ^{31}P ZF spectrum of Fig. 1(a) exhibits a structure with two cusps at approx. 78 and 88 MHz. Such features were identified with independent resonance peaks and assigned to P2 and P1 by Ref. [23]. However, such an attribution is inconsistent with experiments. First, the enhancement factors for the two spectral features differ by a factor of ≈ 3 (η is larger on the higher frequency side), a difference that cannot be reconciled with two close-frequency peaks in a homogeneous magnetic structure, and rather points to nuclei at different positions inside a domain wall [25,39]. Moreover, the two-cusp structure progressively disappears in an applied field large enough to saturate the magnetization. The same figure also shows the 5 K spectra from ^{31}P nuclei in the bulk of domains

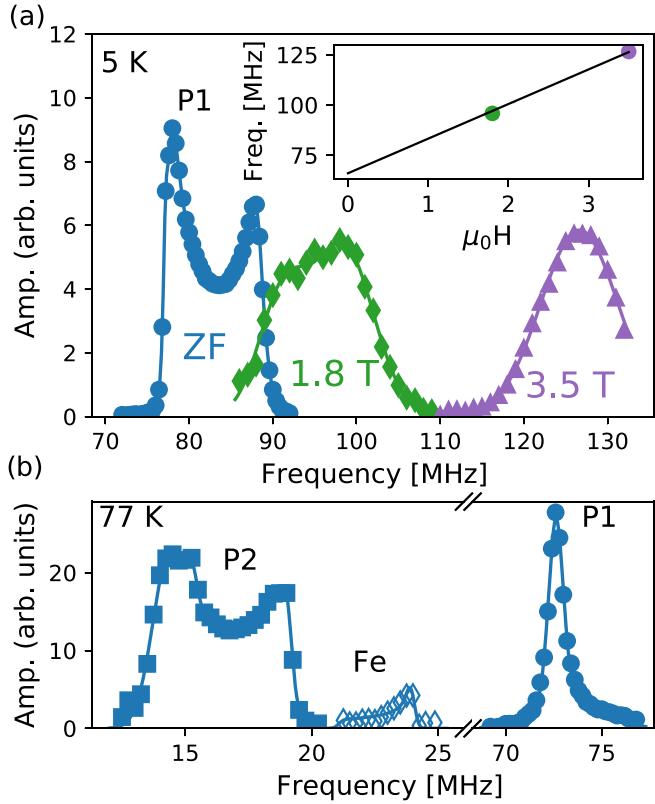


FIG. 1. (a) ^{31}P NMR spectra at $T = 5\text{ K}$ in ZF (domain wall signal) and in applied fields approaching saturation of the magnetization (domain signal). The inset shows the resonant frequency vs applied field, and the black line is a fit described in the main text. (b) ZF NMR spectrum at $T = 77.3\text{ K}$: $^{31}\text{P}2$ (left panel, filled squares), $^{57}\text{Fe}2$ (left panel, empty diamonds) resonance lines, and $^{31}\text{P}1$ resonance (right panel, filled circles). In both panels, the lines are a multi-Gaussian phenomenological fit. Portions of the spectra containing just noise are omitted for clarity.

and in applied field values $\mu_0 H' = 1.8\text{ T}$ and $\mu_0 H'' = 3.5\text{ T}$, corresponding to a nearly saturated state and a practically full saturation of the magnetic moment of polycrystalline Fe_2P , respectively [11].

From H' to H'' , vector composition of the internal field with the external field shifts the resonance frequency as $\delta\nu = \nu'' - \nu' = \mu_0(H'' - H')^{31}\gamma/2\pi$, in agreement with ^{31}P nuclei with a positive hyperfine coupling, while the lineshape tends to a single Gaussian curve at increasing field. It is therefore apparent that these NMR signals constitute a single resonance line, which is assigned to P1 by the DFT calculations detailed below.

The complex lineshape of the ZF spectrum at 5 K seemingly stems from the anisotropic component of the hyperfine coupling and the particular (though unknown) micromagnetic structure of domain walls, whereby spins inside a wall do not sample the solid angle with equal probability. A uniform angle sampling relative to crystal axes, on the contrary, is approached by saturating the magnetization of the polycrystalline specimen. The linewidth of the spectrum in the larger applied field is estimated as $\Delta\nu = 4.6\text{ MHz}$, therefore an rms anisotropic hyperfine field $B_{\text{exp}}^{\text{anis}} = \sqrt{3}\Delta\nu/2\pi/^{31}\gamma =$

$0.46(1)\text{ T}$. The isotropic hyperfine field at this site can be estimated from the first moment of the spectrum $B_{\text{hf}}^{(\text{iso})} = 2\pi\bar{\nu}/^{31}\gamma = 4.7(1)\text{ T}$, a result that, however, suffers from the uncertainty on the details of domain walls. A different estimate is obtained from the linear dependence of the resonance frequency on the applied field, which is obtained from the average weighted by the multi-Gaussian fit in Fig. 1(a). The fit shown in the inset of the same figure, where $\nu(0)$ is the only free parameter, provides $B_{\text{hf}}^{(\text{iso})} = 2\pi\nu(0)/^{31}\gamma = 3.83(4)\text{ T}$.

At higher temperature, the $^{31}\text{P}1$ ZF spectrum evolves into a single narrower peak, again described with a phenomenological multi-Gaussian fit. The two-cusp structure has already disappeared at 77.3 K [Fig. 1(b)], where only a weaker Gaussian shoulder can be detected besides the main peak at 72.6 MHz , and the overall spectral width is estimated as $\Delta\nu = 1.1(1)\text{ MHz}$. The shape of the 77.3 K spectrum, testifying a variation of the anisotropic hyperfine coupling, was checked against different spin-echo excitation conditions (selecting nuclei with different enhancement factors) [41] and was found to be independent of rf pulse amplitude over more than two decades. The narrowing of the ZF spectrum witnesses a decrease of the anisotropic hyperfine coupling of P1 from 5 to 77.3 K . On further warming, the mean resonance frequency vs temperature follows a smooth order parameter curve, with $\bar{\nu}(T)$ values in good agreement with the literature, up to 160 K [23]. Above that temperature, the signal is lost due to exceedingly fast relaxations, and the magnetic transition cannot be probed by NMR.

Lower-frequency resonances, shown in Fig. 1(b), were investigated at 77.3 K . The ZF NMR spectrum features a broad, more intense composite line at $14\text{--}18\text{ MHz}$ and a weaker asymmetric peak at 23.7 MHz . The latter value is in excellent agreement with a ^{57}Fe resonance in the hyperfine field of 17.2 T reported by ^{57}Fe Mössbauer spectroscopy for Fe2 at this temperature [10], which warrants the same assignment for this NMR line. The other broader resonance is, however, incompatible with the ^{57}Fe NMR of Fe1, although such a resonance line is predicted at 15.0 MHz ($B_{\text{hf}} = 10.9\text{ T}$) by the same Mössbauer data. In fact, the same integrated amplitude (after normalization by ν^2) would be expected in that case for the two signals, given the 1:1 Fe occupancy ratio at the two sites. The $14\text{--}18\text{ MHz}$ signal must therefore originate from the resonance of the much more sensitive ^{31}P nuclei in a mean spontaneous field of $0.94(4)\text{ T}$ at the complementary P2 site, while the weaker and overlapped $^{57}\text{Fe}(1)$ line is hidden by it. Our assignment, which contrasts with early literature [23], can be checked against the relative receptivity $R = R'/B_{\text{hf}} = a\gamma^3 B_{\text{hf}}^3 = a\omega^3$ of the two nuclear species. Here $R' = a\gamma^3 B^2$ is the usual dependence of the sensitivity of a nucleus on its abundance a (both isotopic and from site multiplicity) and the local field B in a nonmagnetic substance, whereas in a ferromagnet a further dependency on $B = B_{\text{hf}}$ arises from the enhancement factor [25,39]. After normalization of the spectra by ω^2 (the amplitude correction appropriate for the signals of a single nuclear species), the integrated amplitudes A of the ^{31}P and ^{57}Fe signals should scale relative to each other as $R_n = a\omega$, therefore an expected ratio $^{31}R_n/^{57}R_n = 11$, in fair agreement with the value $^{31}A/^{57}A \approx 16$ that we estimated experimentally. A direct comparison between the ^{31}P NMR amplitudes at P1 and P2 is not possible due to the large

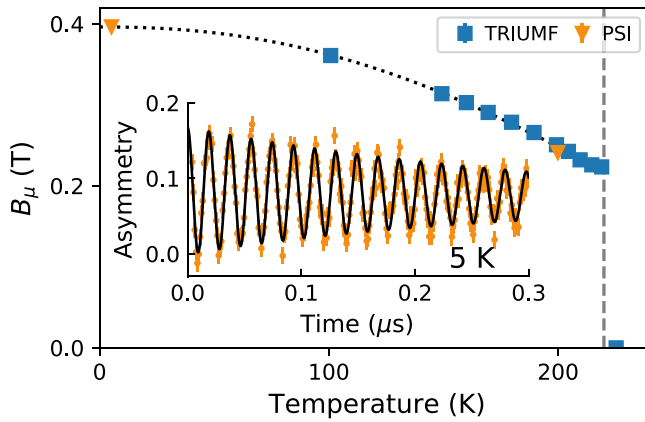


FIG. 2. The local field at the muon site as a function of temperature extracted from fits to ZF- μ SR data collected at TRIUMF (blue squares) and PSI (orange triangles). The vertical dashed line is the Curie temperature (~ 220 K) and the dotted line is a guide to the eye. Inset: ZF- μ SR data at $T = 5$ K. Orange dots and the solid black curve represent the experimental data and best fit, respectively. The coherent oscillations indicate the presence of a well-defined, static magnetic field at the muon site due to the long-range FM order.

difference in frequency, therefore the employment of different resonant circuits.

The $^{31}\text{P}2$ spectrum at 77.3 K exhibits a similar structure to the one observed at 5 K in the $^{31}\text{P}1$ one, which can be explained based on similar arguments. Its linewidth and the P2 rms anisotropic hyperfine field are estimated as $\Delta\nu = 1.8(1)$ MHz and $B_{\text{exp}}^{\text{anis}} = \sqrt{3}\Delta\nu/2\pi/^{31}\gamma = 0.18(1)$ T, hence they are significantly larger, both in absolute and relative terms, than the corresponding P1 values at the same temperature.

B. μ SR

In Fig. 2, we display the ZF- μ SR spectrum collected at 5 K (inset) and the internal field as a function of temperature. The orange dots represent the experimental asymmetry as a function of time. Well-defined oscillations with a single dominant frequency are clearly visible, confirming the presence of a static and fairly uniform magnetic field at the muon stopping site. An excellent fit to the spectrum is obtained using the standard two-component model expected for static internal fields, consisting of an exponentially damped sinusoidal function and a slowly relaxing exponential function, as shown by the black curve in Fig. 2. At 5 K, the best-fit frequency is $\nu = 53.72(1)$ MHz, corresponding to a magnetic field magnitude of $B_{\mu} = \nu/\gamma_{\mu} = 0.3963(1)$ T, where $\gamma_{\mu} = 135.5$ MHz T $^{-1}$ is the gyromagnetic ratio of the muon. Equivalent fits were performed for the ZF spectra collected at temperatures up to $T_c \sim 220$ K, while above T_c a pure exponential decay is observed.

The local static field at the muon site extracted from these fits is displayed as a function of temperature in Fig. 2, with blue squares and orange triangles representing the results from data collected at TRIUMF and PSI, respectively. As the temperature increases toward T_c , the static field steadily decreases, as expected for a magnetic order parameter curve. At approximately 220 K (indicated by the vertical dashed line

TABLE I. *Ab initio* muon sites and contact hyperfine fields. The columns are: site label $\alpha = \text{A-E}$; fractional coordinates in the conventional unit cell [Fe1 at (0.0,0.257,0.0), 3f and Fe2 at (0.0, 0.591, 0.5), 3g]; total energy difference $\Delta E = E_{\alpha} - E_A$; contact hyperfine field.

Label	Wyckoff	(x, y, z)	ΔE (meV)	B_C (T)
A	3g	(0.000, 0.328, 0.500)	0	-0.4274
A*	6k	(0.052, 0.358, 0.500)	0	-0.5022
B	3f	(0.296, 0.296, 0.000)	280	-0.4573
C	2d	(0.333, 0.666, 0.500)	690	-1.7049
D	3f	(0.000, 0.545, 0.009)	760	
E	1a	(0.000, 0.000, 0.000)	1120	

in Fig. 2), however, the static field drops discontinuously to zero, indicating the occurrence of a first-order magnetic transition at this temperature. A fast depolarization (not shown) is observed well above T_c , indicating the presence of short range correlations, in agreement with previous neutron scattering results.

C. Computational results

In order to further characterize the microscopic origin of the experimental results and to validate *ab initio* estimates of hyperfine couplings, we evaluated the internal field at P and the muon sites, after having identified the interstitial position occupied by the latter following a methodology already extensively discussed [42–51]. Five inequivalent candidate muon sites, labeled with letters from A to E in order of increasing total energy, are reported in Table I. The label A* indicates a slightly displaced analogous of site A, with the distance d_{A-A^*} being 0.2 Å. The energy difference between the two is within numerical accuracy, but their distance testifies a rather flat potential energy surface that implies some degree of delocalization of the muon wave function. This has been shown to have limited effects on the local field at the muon site provided that the muon is not diffusing [52].

Notably, the positions A and B are just 0.5 Å and 0.3 Å away from the absolute minimum and the second lowest minimum of the electrostatic potential, while site C corresponds exactly to the position of the third relative minimum of the electrostatic potential. A similar behavior was found in muon site calculations performed on FeCrAs that shares the same space group as Fe₂P [53]. Finally, the largest displacement induced by the muon on the neighboring magnetic atoms is smaller than 0.15 Å.

A similar approach is used to estimate the local field at P sites, where, however, relativistic effects must be considered [54]. The contact term in this case dramatically depends on valence electrons' spin polarization, and an accurate description of the latter is mandatory. The short-range dipolar and orbital contributions are estimated differently by Elk and WIEN2K (see SM [27]), but in both cases B_{OrbSR} is negligible and therefore not reported.

IV. DISCUSSION

The computational description of the hyperfine interaction provides the connection between the details of the magnetic

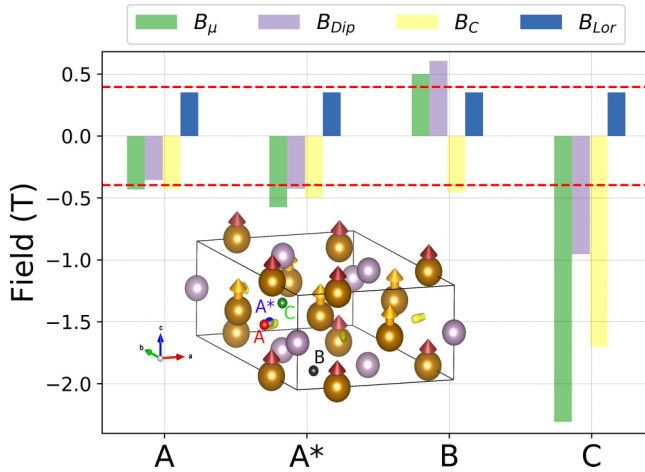


FIG. 3. Bar plot of the contributions to the local field B_μ (green) at four muon sites (A–C), compared with the experimental value (red dashed lines, sign unknown): dipolar (gray), Lorentz (blue), and contact (yellow). Inset: the Fe_2P unit cell with Fe1, Fe2 magnetic moments as orange and red arrows, respectively. Brown and mauve spheres are Fe, P atoms and the muon sites are labeled A–C. The minima of the unperturbed electrostatic potential, U_{\min} , are shown by the yellow isosurfaces at $U_{\min} + 0.2$ eV.

ground state described from first principles and the results from experimental probes of local magnetic moments. In a ZF NMR or μSR experiment performed below T_C , the effective field at the nuclei or muon can be separated into multiple contributions:

$$\mathbf{B}_{\text{Tot}} = \mathbf{B}_{\text{LR}} + \mathbf{B}_{\text{Demag}} + \mathbf{B}_{\text{SR}} \quad (1)$$

$$\mathbf{B}_{\text{LR}} = \mathbf{B}_{\text{Lor}} + \mathbf{B}_{\text{Dip}} \quad (2)$$

$$\mathbf{B}_{\text{SR}} = \mathbf{B}_{\text{C}} + \mathbf{B}_{\text{DipSR}} + \mathbf{B}_{\text{OrbSR}}. \quad (3)$$

The first term in Eq. (1) is the long range (LR) dipolar field which is obtained here in real space using the Lorentz method, in which the magnetic moment of Fe $3d$ orbitals inside a (large) sphere contribute to \mathbf{B}_{Dip} while those outside it are treated as a continuum and add into \mathbf{B}_{Lor} appearing in Eq. (2). $\mathbf{B}_{\text{Demag}}$ is the demagnetization field, which can be neglected in a polycrystalline and multidomain sample, and \mathbf{B}_{SR} is the short range term arising from orbitals localized at the muon or P site, which is further subdivided, in order of appearance in Eq. (3), into the Fermi contact, dipolar, and orbital terms.

For the LR dipolar field we approximate the spin polarization of Fe d orbitals as classical magnetic moments with $m_{\text{Fe1}} = 0.84 \mu_B$ and $m_{\text{Fe2}} = 2.22 \mu_B$, both along c . The occupied orbitals with non-negligible electronic density at the muon sites consist mainly of s character, so relativistic effects can be safely neglected. In this approximation, the short-range contribution [Eq. (3)] is limited to the contact term, which is estimated from the electronic spin polarization at the muon position \mathbf{R}_l as $B_{\text{SR}} = \frac{2}{3} \mu_0 \mu_B \rho_s(\mathbf{R}_l)$ [45,55] where $\rho_s(\mathbf{R}_l)$ is the spin density at the muon site. We can therefore compute $\mathbf{B}_{\text{Tot}}(\mathbf{R}_l)$ entirely from first principles; the results are shown in Fig. 3 [56]. The long range dipolar contributions are negligible for both the lowest energy sites A and B, where the local field originates from the Fermi contact term. The comparison with

TABLE II. Hyperfine fields (Tesla) at the P nuclei in the low temperature FM phase. Positive contact fields are along the direction of Fe- d orbital spin polarization. The two values reported for B_C in the Elk rows are the results of two different algorithms (see SM [27]). The anisotropic contribution is separated in B_{DipSR} , obtained by DFT (short range), and the complement B_{Dip} , from distant dipole sums (the Lorentz contribution is 0.35 T). The definition of the two experimental values is given in the text.

Code	Nuc.	B_C	$B_{\text{DipSR}}^{\text{anis}}$	$B_{\text{Dip}}^{\text{anis}}$	$B_{\text{exp}}^{\text{iso}}$	$\sqrt{5/2} B_{\text{exp}}^{\text{anis}} $
WIEN2K	P1	3.8	-1.0	+0.11	3.83(4) ^a	0.73(2) ^a
	P2	0.3	0.2	-0.19	0.94(4) ^b	0.28(2) ^b
Elk	P1	4.0/3.2	-0.8	+0.11	3.83(4) ^a	0.73(2) ^a
	P2	0.2/0.7	0.1	-0.19	0.94(4) ^b	0.28(2) ^b

^aData from applied field NMR.

^bData from ZF NMR.

the experimentally measured local field is excellent for both sites, with the former showing slightly better agreement.

The calculated hyperfine field at P1 and P2 sites shown in Table II provides the attribution of the NMR peaks. The contact term accurately reproduces the experimental bulk $B_{\text{hf}}^{\text{(iso)}}$ for P1, while the comparison for P2 is seemingly less accurate. The field shift of a signal originating from a domain wall, like our zero field signal for P2, is of the order of the long range dipolar contribution. In view of the unknown domain wall structure, this provides a systematic error in our zero field data analysis. This error can also be approximately quantified by comparing the local field obtained from bulk and wall signals for P2, which is 0.9 T. This systematic error has the same magnitude as the uncertainty of the computational estimate, as is evident from the comparison of the values referring to equivalent quantities appearing in Table II, so that the present analysis of the experimental data is still perfectly adequate for our comparison purpose. In light of this, the small deviation between the predicted and experimental isotropic contribution at P2 is not surprising.

The analysis of the anisotropic part requires more care. In Table II, the experimental $B_{\text{exp}}^{\text{anis}}$, which represents the average of the anisotropic broadening over all directions, is multiplied by $\sqrt{5/2}$ in order to compare it with the anisotropic contributions generated by the short-range and long-range dipolar interactions described *ab initio*. The experimental values reported for P2 are small, and the systematic error due to the lack of domain wall description makes it difficult to draw meaningful comparisons. On the other hand, in applied field, at saturation, B_{Lor} and B_{Demag} cancel out and, as a consequence, for Fe_2P , only B_{DipSR} and B_{Dip} contribute to the anisotropic part. Good quantitative agreement is obtained in this case for P1.

V. CONCLUSIONS

Summarizing, we investigated the FM phase of Fe_2P using in-field and zero-field ^{31}P NMR and μSR , characterizing in detail both experimental signals in the low temperature magnetic phase. These results are interpreted by means of electronic structure simulations that unveiled the interstitial position occupied by the muon and provided hyperfine

parameters for P nuclei and the muon, accurately reproducing the experimental measurements. An excellent agreement between theory and experiment is reported, and our results introduce a framework for the analysis of future experiments on Fe₂P alloys of technological interest.

ACKNOWLEDGMENTS

We thank Gerald Morris, Bassam Hitti, and Donald Arseneau for their support at the μ SR beamline at TRIUMF, as well as Nicholas Ducharme, Alexander Shaw, Jacob Hughes, and Alec Petersen for their assistance collecting the data.

We acknowledge the College of Physical and Mathematical Sciences at Brigham Young University for providing support to travel to TRIUMF. Analysis of the μ SR data was supported by the United States Department of Energy, Office of Science, through Award No. DE-SC0021134. We thank Francesco Cugini for fruitful discussion and we are in debt to John Kay Dewhurst and the developers of the Elk code for their prompt support and availability. We acknowledge ISCRAC allocation at CINECA (Award No. HP10CJLG7W) and computer time allocations at SCARF and University of Parma. This work is based on experiments performed at the Swiss Muon Source S μ S, Paul Scherrer Institute, Villigen, Switzerland.

-
- [1] R. Hussain, F. Cugini, S. Baldini, G. Porcari, N. Sarzi Amadè, X. F. Miao, N. H. van Dijk, E. Brück, M. Solzi, R. De Renzi, and G. Allodi, *Phys. Rev. B* **100**, 104439 (2019).
- [2] F. Guillou, Sun-Liting, O. Haschuloo, Z. Ou, E. Brück, O. Tegus, and H. Yibole, *J. Alloys Compd.* **800**, 403 (2019).
- [3] F. Guillou, G. Porcari, H. Yibole, N. van Dijk, and E. Brück, *Adv. Mater.* **26**, 2671 (2014).
- [4] A. Kitanovski, *Adv. Energy Mater.* **10**, 1903741 (2020).
- [5] D. Dzekan, A. Waske, K. Nielsch, and S. Fähler, *APL Mater.* **9**, 011105 (2021).
- [6] E. Brück, *J. Phys. D* **38**, R381 (2005).
- [7] N. T. Trung, L. Zhang, L. Caron, K. H. J. Buschow, and E. Brück, *Appl. Phys. Lett.* **96**, 172504 (2010).
- [8] N. H. Dung, Z. Q. Ou, L. Caron, L. Zhang, D. T. C. Thanh, G. A. de Wijs, R. A. de Groot, K. H. J. Buschow, and E. Brück, *Adv. Energy Mater.* **1**, 1215 (2011).
- [9] O. Tegus, E. Brück, K. Buschow, and F. R. de Boer, *Nat. Mater.* **415**, 150 (2002).
- [10] R. Wäppling, L. Häggström, T. Ericsson, S. Devanarayanan, E. Karlsson, B. Carlsson, and S. Rundqvist, *J. Solid State Chem.* **13**, 258 (1975).
- [11] L. Caron, M. Hudl, V. Höglin, N. H. Dung, C. P. Gomez, M. Sahlberg, E. Brück, Y. Andersson, and P. Nordblad, *Phys. Rev. B* **88**, 094440 (2013).
- [12] I. A. Zhuravlev, V. P. Antropov, A. Vishina, M. van Schilfhaarde, and K. D. Belashchenko, *Phys. Rev. Materials* **1**, 051401(R) (2017).
- [13] B. Carlsson, M. Gölin, and S. Rundqvist, *J. Solid State Chem.* **8**, 57 (1973).
- [14] D. Scheerlinck and E. Legrand, *Solid State Commun.* **25**, 181 (1978).
- [15] H. Fujii, S. Komura, T. Takeda, T. Okamoto, Y. Ito, and J. Akimitsu, *J. Phys. Soc. Jpn.* **46**, 1616 (1979).
- [16] J. Tobola, M. Bacmann, D. Fruchart, S. Kaprzyk, A. Koumina, S. Niziol, J.-L. Soubeyroux, P. Wolfers, and R. Zach, *J. Magn. Mater.* **157-158**, 708 (1996).
- [17] A. Koumina, M. Bacmann, D. Fruchart, J. Soubeyroux, P. Wolfers, J. Tobola, S. Kaprzyk, S. Niziol, M. Mesnaoui, and R. Zach, *Ann. Chim. Sci. Mater.* **23**, 177 (1998).
- [18] H. Fujii, Y. Uwatoko, K. Motoya, Y. Ito, and T. Okamoto, *J. Phys. Soc. Jpn.* **57**, 2143 (1988).
- [19] X. F. Miao, L. Caron, J. Cedervall, P. C. M. Gubbens, P. Dalmás de Réotier, A. Yaouanc, F. Qian, A. R. Wildes, H. Luetkens, A. Amato, N. H. van Dijk, and E. Brück, *Phys. Rev. B* **94**, 014426 (2016).
- [20] N. H. Dung, L. Zhang, Z. Q. Ou, L. Zhao, L. van Eijck, A. M. Mulders, M. Avdeev, E. Suard, N. H. van Dijk, and E. Brück, *Phys. Rev. B* **86**, 045134 (2012).
- [21] J. Cedervall, M. S. Andersson, E. K. Delczeg-Czirjak, D. Iuşan, M. Pereiro, P. Roy, T. Ericsson, L. Häggström, W. Lohstroh, H. Mutka, M. Sahlberg, P. Nordblad, and P. P. Deen, *Phys. Rev. B* **99**, 174437 (2019).
- [22] R. Wäppling, O. Hartmann, E. Wäckelgård, and T. Sundqvist, *J. Magn. Mater.* **50**, 347 (1985).
- [23] E. Koster and B. G. Turrell, *J. Appl. Phys.* **42**, 1314 (1971).
- [24] G. Allodi, A. Banderini, R. D. Renzi, and C. Vignali, *Rev. Sci. Instrum.* **76**, 083911 (2005).
- [25] P. C. Riedi, *Hyperfine Interact.* **49**, 335 (1989).
- [26] I. Oliveira and A. Guimarães, *J. Magn. Mater.* **170**, 277 (1997), cited by Ref. [8].
- [27] See Supplemental Material at <http://link.aps.org/supplemental/10.1103/PhysRevMaterials.5.044411> for a description of the experimental setting and the computational details used to produce the results shown in the main text.
- [28] A. Suter and B. M. Wojek, *Phys. Proc.* **30**, 69 (2012).
- [29] J. Senateur, A. Rouault, R. Fruchart, J. Capponi, and M. Perroux, *Mater. Res. Bull.* **11**, 631 (1976).
- [30] E. K. Delczeg-Czirjak, L. Delczeg, M. P. J. Punkkinen, B. Johansson, O. Eriksson, and L. Vitos, *Phys. Rev. B* **82**, 085103 (2010).
- [31] S. S. Bhat, K. Gupta, S. Bhattacharjee, and S.-C. Lee, *J. Phys.: Condens. Matter* **30**, 215401 (2018).
- [32] S. Ishida, S. Asano, and J. Ishida, *J. Phys. F* **17**, 475 (1987).
- [33] P. Giannozzi, S. Baroni, N. Bonini, M. Calandra, R. Car, C. Cavazzoni, D. Ceresoli, G. L. Chiarotti, M. Cococcioni, I. Dabo, A. D. Corso, S. de Gironcoli, S. Fabris, G. Fratesi, R. Gebauer, U. Gerstmann, C. Gougoussis, A. Kokalj, M. Lazzeri, L. Martin-Samos, N. Marzari, F. Mauri, R. Mazzarello, S. Paolini, A. Pasquarello, L. Paulatto, C. Sbraccia, S. Scandolo, G. Sclauzero, A. P. Seitsonen, A. Smogunov, P. Umari, and R. M. Wentzcovitch, *J. Phys.: Condens. Matter* **21**, 395502 (2009).
- [34] P. Giannozzi, O. Andreussi, T. Brumme, O. Bunau, M. Buongiorno Nardelli, M. Calandra, R. Car, C. Cavazzoni, D. Ceresoli, M. Cococcioni *et al.*, *J. Phys.: Condens. Matter* **29**, 465901 (2017).
- [35] K. Dewhurst, S. Sharma, L. Nordstrom, F. Cricchio, O. Grånäs, H. Gross, C. Ambrosch-Draxl, C. Persson, F. Bultmark, and C. Brouder, The elk code, version 6.8.21 (2019).
- [36] K. Schwarz and P. Blaha, *Comput. Mater. Sci.* **28**, 259 (2003).

- [37] P. Giannozzi, O. Baseggio, P. Bonfà, D. Brunato, R. Car, I. Carnimeo, C. Cavazzoni, S. de Gironcoli, P. Delugas, F. Ferrari Ruffino, A. Ferretti, N. Marzari, I. Timrov, A. Urru, and S. Baroni, *J. Chem. Phys.* **152**, 154105 (2020).
- [38] P. Novák, H. Štěpánková, J. Englich, J. Kohout, and V. A. M. Brabers, *Phys. Rev. B* **61**, 1256 (2000).
- [39] P. Panissod and C. Mény, *Appl. Magn. Reson.* **19**, 447 (2000).
- [40] The enhancement factor of nuclei in the bulk of domains can be estimated as $\eta_d = B_{hf}/B_{an} < 2$ [25,39] from the known value of the anisotropy field B_{an} on the order of several Tesla in Fe₂P [11].
- [41] P. Panissod, in *Frontiers in Magnetism of Reduced Dimension Systems*, edited by V. G. Bar'yakhtar, and P. E. Wigen, NATO ASI Series (3. High Technology) Vol. 49 (Springer, Dordrecht, 1998).
- [42] F. Bernardini, P. Bonfà, S. Massidda, and R. De Renzi, *Phys. Rev. B* **87**, 115148 (2013).
- [43] J. S. Möller, P. Bonfà, D. Ceresoli, F. Bernardini, S. J. Blundell, T. Lancaster, R. D. Renzi, N. Marzari, I. Watanabe, S. Sulaiman, and M. I. Mohamed-Ibrahim, *Phys. Scr.* **88**, 068510 (2013).
- [44] P. P. Bonfà, F. Sartori, and R. De Renzi, *J. Phys. Chem. C* **119**, 4278 (2015).
- [45] I. J. Onuorah, P. Bonfà, and R. De Renzi, *Phys. Rev. B* **97**, 174414 (2018).
- [46] F. Lang, L. Jowitt, D. Prabhakaran, R. D. Johnson, and S. J. Blundell, *Phys. Rev. B* **100**, 094401 (2019).
- [47] S. N. A. Ahmad, S. Sulaiman, D. F. H. Baseri, L. S. Ang, N. Z. Yahaya, H. Arsad, and I. Watanabe, *J. Phys. Soc. Jpn.* **89**, 014301 (2020).
- [48] J. P. Perdew, K. Burke, and M. Ernzerhof, *Phys. Rev. Lett.* **77**, 3865 (1996).
- [49] H. J. Monkhorst and J. D. Pack, *Phys. Rev. B* **13**, 5188 (1976).
- [50] N. Marzari, D. Vanderbilt, A. De Vita, and M. C. Payne, *Phys. Rev. Lett.* **82**, 3296 (1999).
- [51] P. E. Blöchl, *Phys. Rev. B* **50**, 17953 (1994).
- [52] I. J. Onuorah, P. Bonfà, R. De Renzi, L. Monacelli, F. Mauri, M. Calandra, and I. Errea, *Phys. Rev. Materials* **3**, 073804 (2019).
- [53] B. M. Huddart, M. T. Birch, F. L. Pratt, S. J. Blundell, D. G. Porter, S. J. Clark, W. Wu, S. R. Julian, P. D. Hatton, and T. Lancaster, *J. Phys.: Condens. Matter* **31**, 285803 (2019).
- [54] S. Blügel, H. Akai, R. Zeller, and P. H. Dederichs, *Phys. Rev. B* **35**, 3271 (1987).
- [55] C. G. Van de Walle and P. E. Blöchl, *Phys. Rev. B* **47**, 4244 (1993).
- [56] P. Bonfà, I. J. Onuorah, and R. De Renzi, *JPS Conf. Proc.* **21**, 011052 (2018).